

Facile Synthesis of Efficient Luminogens with AIE Features for Three-Photon Fluorescence Imaging of the Brain through the Intact Skull

Wei Qin, Nuernisha Alifu, Jacky W. Y. Lam, Yuhan Cui, Huifang Su, Guodong Liang,* Jun Qian,* and Ben Zhong Tang*

Visualization of the brain in its native environment is important for understanding common brain diseases. Herein, bright luminogens with remarkable aggregation-induced emission (AIE) characteristics and high quantum yields of up to 42.6% in the solid state are synthesized through facile reaction routes. The synthesized molecule, namely BTF, shows ultrabright far-red/near-infrared emission and can be fabricated into AIE dots by a simple nanoprecipitation procedure. Due to their high brightness, large Stokes shift, good biocompatibility, satisfactory photostability, and large three-photon absorption cross section, the AIE dots can be utilized as efficient fluorescent nanoprobes for in vivo brain vascular imaging through the intact skull by a three-photon fluorescence microscopy imaging technique. This is the first example of using AIE dots for the visualization of the cerebral stroke process through the intact skull of a mouse with high penetration depth and good image contrast. Such good results are anticipated to open up a new venue in the development of efficient emitters with strong nonlinear optical effects for noninvasive bioimaging of living brain.

of its traditional near-infrared (NIR, 700–1000 nm) excitation and low tendency for photobleaching.^[4] Through optical access to the mouse brain by common craniotomy, researchers can obtain clear images through 2PF microscopy.^[5] However, even with the help of a cranial window, 2PF imaging is generally limited to image the superficial depth due to light scattering of the excitation beam in biosubstrates.^[6] Moreover, such invasive operation is far from satisfactory in practical application owing to the permanent loss of integral skull that results in a low survival rate of animal after operation. Furthermore, the perturbation of native environment and inflammation of the brain tissue are unavoidable destructive interference, which leads to compromised imaging quality.^[7] Therefore, the observation of brain in its native

Fluorescence imaging provides a new platform for real-time tracking of complicated biological process with high sensitivity and fast response.^[1] Blood vasculature is the crucial component of the circulatory system^[2] and the application of fluorescent nanoprobes for the visualization of blood vessels of brain in vivo is important to gain insight into the common diseases of brain.^[3] Two-photon fluorescence (2PF) microscopy is commonly utilized for in vivo deep-tissue imaging because

environment with a noninvasive method is highly desirable for research on brain disease.^[8]

To solve the abovementioned problems, three-photon fluorescence (3PF) microscopy imaging is developing rapidly as an effective imaging modality.^[9] Unlike conventional 2PF imaging, 3PF imaging technique utilizes higher-order nonlinear localized excitation at NIR-II region (1000–1700 nm) to enable significant improvement in penetration depth, spatiotemporal resolution,

Dr. W. Qin, Y. Cui, Prof. G. Liang
PCFM and GDHPPC Labs
School of Materials Science and Engineering
Sun Yat-sen University
Guangzhou 510275, China
E-mail: lgdong@mail.sysu.edu.cn

Dr. N. Alifu, Prof. J. Qian
State Key Laboratory of Modern Optical Instrumentations
Center for Optical and Electromagnetic Research
JORCEP (Sino-Swedish Joint Research Center of photonics)
Zhejiang University
Hangzhou 310058, China
E-mail: qianjun@zju.edu.cn

Dr. N. Alifu
College of Medical Engineering and Technology
Xinjiang Medical University
Urumqi 830011, China

Dr. J. W. Y. Lam, Prof. B. Z. Tang
Department of Chemistry
Hong Kong Branch of Chinese National Engineering Research Centre
for Tissue Restoration and Reconstruction
Hong Kong University of Science and Technology
Clear Water Bay, Kowloon, Hong Kong
E-mail: tangbenz@ust.hk

Dr. H. Su
Department of Orthopaedic Surgery
The First Affiliated Hospital of Zhengzhou University
Zhengzhou, Henan Province 450052, China

 The ORCID identification number(s) for the author(s) of this article can be found under <https://doi.org/10.1002/adma.202000364>.

DOI: 10.1002/adma.202000364

and signal-to-background ratio (SBR).^[9] Taking the full advantage of 3PF microscopy imaging, scientists have made original works based on commercial fluorescent proteins in imaging the structure and function of a mouse brain with high contrast.^[10] Despite these advantages, a major limitation of 3PF imaging is the lack of organic dyes with large three-photon absorption cross section and high fluorescence quantum efficiency.^[11]

To date, various types of three-photon fluorescent bioprobes have been developed, including fluorescent proteins,^[12] inorganic quantum dots (QDs),^[13] and organic dyes.^[14] Unfortunately, fluorescent proteins are unstable to laser irradiation and enzyme degradation, while inorganic QDs suffer from irregular blinking and potential toxicity in biological environment.^[15] On the other hand, organic fluorophores with tunable absorption and emission wavelengths can circumvent the abovementioned problems owing to the satisfactory stability and good compatibility.^[16] The conventional design of organic multiphoton absorbing materials for 3PF microscopy imaging is mainly based on the introduction of strong electron-donating and electron-accepting moieties in the molecular structures.^[14] However, most organic chromophores are constructed from hydrophobic skeletons and suffer from aggregation-caused quenching (ACQ) effect in the aggregated state with weakened fluorescence efficiency and compromised imaging performance.^[17] To overcome the limitations of ACQ chromophores, organic luminogens with aggregation-induced emission (AIE) characteristics have been designed and synthesized for different purposes.^[18] The active AIE research in the past decade has generated a large variety of AIE luminogens (AIEgens), and most of them are based on tetraphenylethylene (TPE) skeleton.^[19] However, due to the difficulty in delicate molecular design and chemical synthesis, few AIEgens with large absorption cross sections are reported for 3PF bioimaging applications.^[20] It is still challenging to design and synthesize efficient AIE luminogens with simple structures for 3PF bioimaging.

Stroke is a sudden onset disease of brain. It occurs when the supply of blood to part of the brain is either interrupted or suddenly decreased to normally lead to permanent brain damage or death.^[21] Thus, its relevant studies are of great importance for fundamental research and clinical diagnosis.^[22] Common nonfluorescence-based methods for brain imaging are based on bulky and expensive modern instruments, such as computed tomography and magnetic resonance imaging.^[23] However, these methods possess several disadvantages, such as low spatial resolution and high energy radiation.^[24] On the other hand, cerebral thrombosis is generally associated with abnormal conditions in blood flow. Through the use of 3PF nanoprobe as hemodynamic indicators in blood flow, the detailed process of cerebral thrombosis can be effectively visualized and monitored.

With these ideas in mind, we have designed and synthesized non-TPE-based luminogens, namely BBF and BTF. These molecules possess simple structures and are efficient solid-state AIE emitters with high quantum yields. BTF with efficient far-red/near-infrared (FR/NIR) emission can be formulated into AIE nanodots with a high quantum efficiency of 36.1%, a large Stokes shift, satisfactory biocompatibility, good photostability, and large three-photon absorption cross section. They can be utilized as ultrabright fluorescent probes for 3PF imaging of

blood vasculature through the intact skull of mouse with high sensitivity. This is the first example of using AIE dots for the visualization of cerebral thrombosis process through the intact skull of mouse with high penetration depth and good image contrast. Thus, this is expected to inspire new insights into the development of efficient NIR emitters with an outstanding 3PF effect for biomedical applications.

BBF and BTF were facily prepared using inexpensive commercial products according to synthetic pathways in **Figure 1** and Scheme S1 (Supporting Information). Their chemical structures were fully confirmed by nuclear magnetic resonance, high-resolution mass spectrometry, and single-crystal X-ray diffraction (Figures S1–S6, Supporting Information). BBF can be facily prepared by a one-step reaction route (Scheme S1, Supporting Information). Incorporation of diphenylamine (DPA) derivatives into the BBF structure generates a new adduct abbreviated as BTF (Figure 1A) with strong electron-donating triphenylamine (TPA) carrying *tert*-butyl (*t*-Bu) groups and electron-accepting fumaronitrile (FN) moiety. Such a donor–acceptor (D–A) structure is expected to endow BTF with the FR/NIR emission and distinct multiphoton absorption. Moreover, BTF contains more freely rotatable phenyl rings and *t*-Bu groups to favor the consumption of excited-state energy in the solution state through active intramolecular motions. Such motions are restricted in the aggregated state, which enables the excitons to decay radiatively to facilitate the AIE process.^[25] In addition, the twisted TPA moieties and the bulky *t*-Bu groups of BTF hinder the formation of strong π – π stacking interactions. These collective factors enable BTF to show long wavelength emission and high quantum efficiency.

BBF and BTF show good solubility in common organic solvents, such as toluene (Tol), 1,4-dioxane (DO), dichloromethane (DCM), tetrahydrofuran (THF), and ethyl acetate (EA), but are not soluble in water. The absorption spectra of BBF and BTF measured in THF are peaked at 345 and 498 nm, respectively (Figure S7, Supporting Information) and vary slightly by solvent polarity (Figures S8A and S9A, Supporting Information). The photoluminescence (PL) spectra of BBF and BTF in solvents with different polarities are demonstrated in Figures S8 and S9 (Supporting Information). When the solvent polarity is increased from non-polar Tol to polar EA, the PL maximum of BBF varies in a small extent (≈ 4 nm). Under the same condition, the emission of BTF shifts bathochromically by 20 nm from 629 to 649 nm. This reveals that after introduction of DPA into the molecular structure of BBF, the emission of BTF is significantly red-shifted with positive solvatochromism due to the remarkable intramolecular charge transfer (ICT) effect.^[26] To investigate the effects of aggregation and solvent polarity on the emission process of BBF and BTF, their PL spectra in THF/water mixtures with different water fractions (f_w) were measured. BBF emits a weak blue fluorescence in pure THF. The PL intensity starts to increase at a high water content of 80% and reaches its maximum value at 95% water content, which is 20-fold higher than that in pure THF (Figure S10, Supporting Information). BTF, on the other hand, emits a weak fluorescence with a maximum at 647 nm in pure THF (Figure 1C). When a small amount of water ($f_w \leq 50\%$) was added to the THF solution of BTF, its emission is weakened

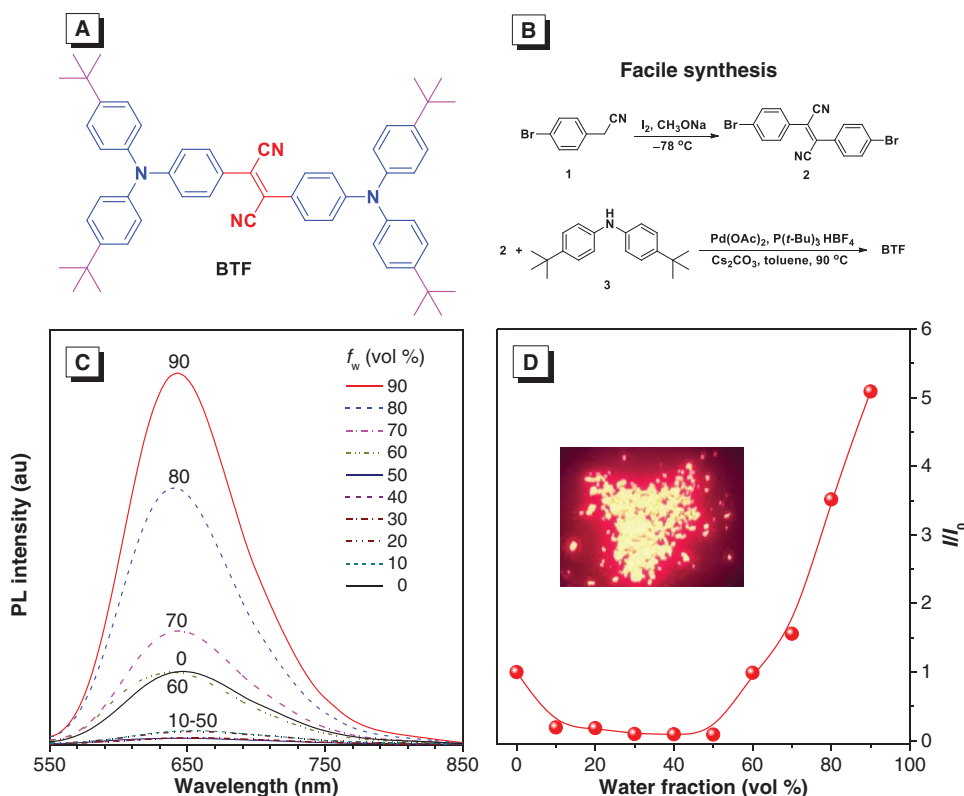


Figure 1. A) Chemical structure and B) synthetic pathway of BTF. C) PL spectra of BTF in THF/water mixtures with different water fractions (f_w). D) Plot of the relative PL intensity (I/I_0) versus the composition of the THF/water mixtures of BTF. I_0 = emission intensity in pure THF. Solution concentration = 10×10^{-6} M; Excitation wavelength = 500 nm. Inset: fluorescence photograph of BTF powders taken under 365 nm UV irradiation.

and red-shifted to 650 nm due to the typical twisted intramolecular charge transfer (TICT) effect.^[27] TICT is a common photophysical phenomenon in organic molecules constructed from electron donating and accepting units. In polar environment, these molecules undergo rapid intramolecular electron transfer from the donor to the acceptor moiety, and intramolecular D–A conformation change from a coplanar structure to a twisted conformation.^[27] However, the TICT effect and the AIE property are competitive factors for determination of the PL intensity. Further increment of the water content ($f_w \geq 60\%$), BTF molecules form nanoaggregates due to their hydrophobic effect. Such hydrophobic environment in the nanoaggregates alleviates the TICT effect and enables the AIE effect more pronounced as the dominant factor, leading to the increased PL intensity of BTF mixture.^[28] The higher the water fraction, the stronger will be the fluorescence intensity. At $f_w = 90\%$, the maximum PL intensity is attained, which is fivefold of that in pure THF solution (Figure 1D). Clearly, BTF is AIE-active. The same conclusion is also drawn from the quantitative measurement. The fluorescence quantum efficiency (Φ_F) of BBF and BTF in pure THF solution is 0.2% and 2.7%, which dramatically enhances to 39.8% and 42.6%, respectively, in the solid state (Table S1, Supporting Information). The lifetimes of BBF and BTF powders are measured to be 1.9 and 2.0 ns, respectively, demonstrating the fluorescence nature of the light emission rather than long-lived delayed fluorescence or phosphorescence (Figure S11, Supporting Information).

To obtain further insight into the effect of the molecular structures on fluorescence emission of BBF and BTF, their single crystals were grown and analyzed by X-ray diffraction. The crystal data and the collection of parameters were summarized in Tables S2–S4 (Supporting Information). As shown by the crystal structures in Figure S12 (Supporting Information), the cyano groups of BTF adopt a *trans*-conformation. The large dihedral angle of 177.05° between the cyano group and the central double bond reveals that they are intrinsically planar and well conjugated with good π -electron delocalization (Figure 2A). On the other hand, the propeller-shaped TPA unit is twisted from the central olefin plane. The torsion angle between the central double bond and the adjacent phenyl rings is measured to be 36.31° . The dihedral angles of the phenyl rings of TPA are calculated to be 66.54° , 56.02° , and 75.45° (Figure 2A). In addition, the *t*-Bu groups and adjacent phenyl rings are also nonplanar with torsion angles from 4.71° to 64.43° (Table S5, Supporting Information). BTF packs in the triclinic crystal system, from which two representative dimers are extracted to study the molecular packing. It is interesting to note that the hydrogen atoms of benzene rings and *t*-Bu groups participate in multiple C–H \cdots N and C–H \cdots π interactions in BTF crystals (Figure 2B,C). Multiple strong C–H \cdots N interactions are present in crystals with short hydrogen bonding distances (e.g., 2.957, 3.054, and 3.243 Å in dimer 1 and 2.782, 3.220, and 3.281 Å in dimer 2). Abundant C–H \cdots π interactions exist in adjacent molecules with short bond lengths (e.g., 3.164, 3.362, and 3.381 Å). Such abundant

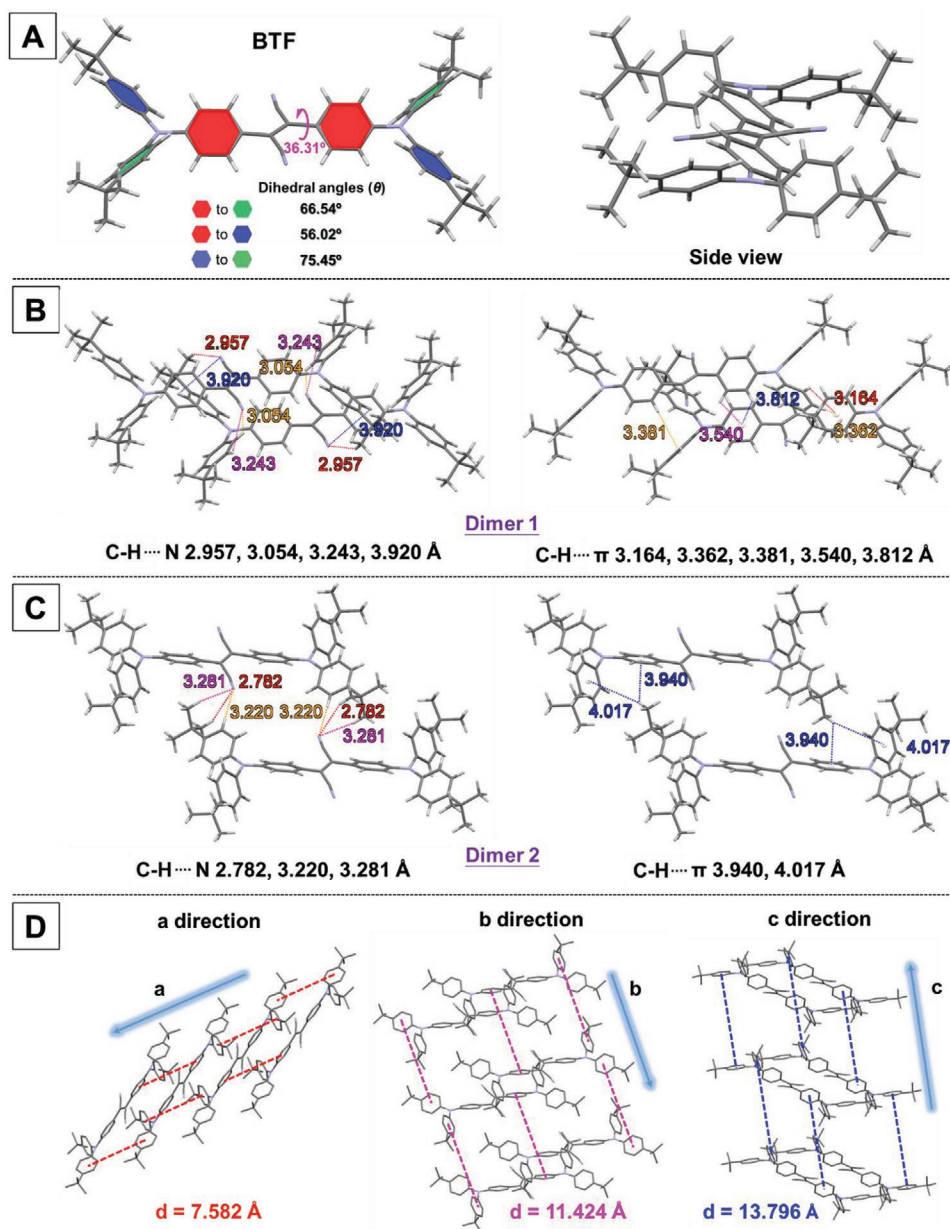


Figure 2. A) Single crystal structure of BTF. B,C) Two dimers extracted from the single-crystal structure of BTF with bond lengths. D) Molecular stacking structures along the *a*, *b*, and *c* directions in BTF crystals.

interactions between adjacent molecules greatly restrict the molecular motions and efficiently suppress the nonradiative relaxation of excitons to enable the molecules to emit intense FR/NIR emission in crystals. It is noteworthy that the cooperation of multiple interactions enables the BTF molecules to arrange in a slipped parallel manner within the crystals along the *a*, *b*, and *c* directions with intermolecular distances of 7.582, 11.424, and 13.796 Å, respectively (Figure 2D). Similar to BTF, BBF also adopts a twisted conformation in the crystal state owing to the nonplanarity of the *t*-Bu groups (Figure S13 and Tables S6–S8, Supporting Information). It also packs in triclinic crystal system, where multiple C–H...N and C–H... π interactions exist in the crystal lattice (Figure S14, Supporting

Information). A similar slipped parallel molecular arrangement with intermolecular distances of 7.409, 9.561, and 14.750 Å was observed (Figure S14, Supporting Information).

To understand the electronic distributions and molecular geometries of BBF and BTF at the molecular level, density functional theory calculations were carried out (Figure S15, Supporting Information). The electron clouds of the highest occupied molecular orbital (HOMO) and the lowest unoccupied molecular orbital (LUMO) of BBF are dispersed on the whole molecule. In contrast, the HOMO of BTF is contributed by orbitals of the FN core and the TPA moieties. The electron clouds of the LUMO, on the other hand, are concentrated on the 2,3-diphenylfumaronitrile unit. The remarkable difference

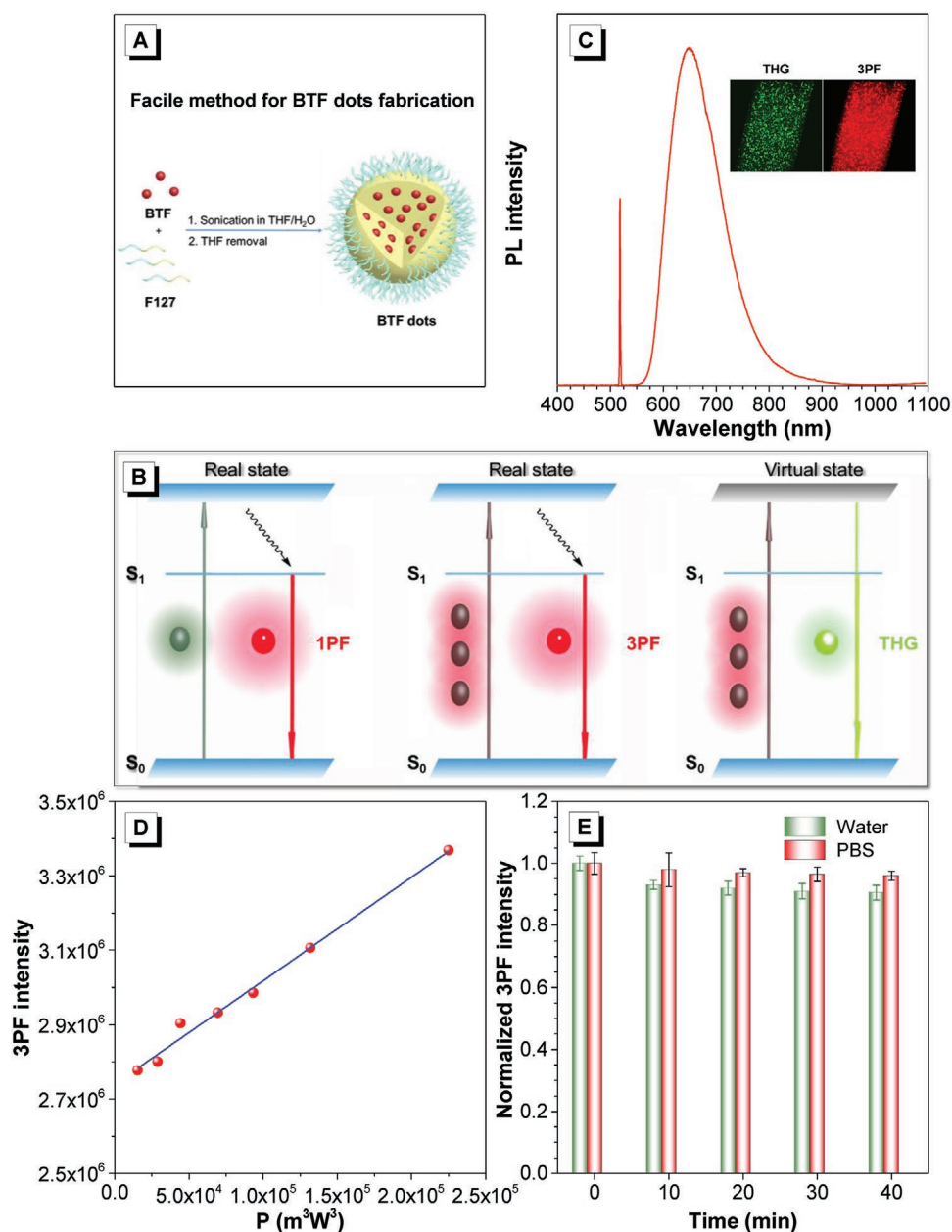


Figure 3. A) Illustration of the formulation process of BTF dots using F127 as the polymer matrix. B) Schematic illustration of 1PF, 3PF, and THG processes. C) Nonlinear optical property of BTF in aqueous dispersion measured under 1550 nm fs laser excitation. Inset: THG and 3PF images of BTF aqueous dispersion in capillary glass tube. D) Power dependence relationship of the fluorescence intensity of the BTF dots under 1550 nm fs laser excitation. E) 3PF intensity of the BTF dots at different time points under continuous laser irradiation at 1550 nm.

in electron distribution of HOMO and LUMO of BTF reveals an intrinsic ICT feature, which is consistent with the result from Figure S9 (Supporting Information).

The FR/NIR emission of BTF with a high Φ_F in the aggregated state prompts us to study its bioimaging application. To endow the hydrophobic BTF with good water dispersibility in aqueous media, amphiphilic polymeric Pluronic F-127 was applied as biocompatible encapsulation agent to formulate BTF dots (Figure 3A). In aqueous solution, the lipophilic part of Pluronic F-127 and AIE molecules form the nanodot core. While the hydrophilic part extends into water to form outer

shell. The size of the BTF dots in aqueous solution was measured by dynamic light scattering (DLS) with a hydrodynamic diameter of 128 nm (Figure S16A, Supporting Information), which was further confirmed by scanning electron microscopy (SEM). The BTF dots display an absorption maximum at 500 nm in aqueous solution, which well fits with the commercial laser excitation at 515 nm. The PL spectrum of the BTF dots is peaked at the red region (645 nm) and well extends to the NIR region (800 nm) (Figure S16B, Supporting Information). The BTF dots enjoy a larger Stokes shift (>130 nm) than those of conventional organic dyes (normally <25 nm), which is

beneficial for high-contrast bioimaging applications due to the lesser tendency for emission quenching by self-absorption.^[29] The fluorescence quantum yield (Φ_F) of the BTF dots was determined to be 36.1% by using 4-(dicyanomethylene)-2-methyl-6-(*p*-dimethylaminostyryl)-4*H*-pyran ($\Phi_F = 43\%$ in methanol) as standard.

The BTF dots possess a long-term stability shown in Figure S17 (Supporting Information). Their PL spectra remain almost unchanged even their suspension solutions in phosphate buffer saline (PBS) are stored at room temperature for a long time. The HeLa cells incubated with BTF dots exhibit no fluorescence, indicative of little or no endocytosis (Figure S18, Supporting Information). The cytotoxicity of the BTF dots was evaluated by their incubation with HeLa cells at different concentrations (12.5, 25, 50, and 100 $\mu\text{g mL}^{-1}$) for 24 h (Figure S19, Supporting Information). The cell viability all remains at above 95%, revealing the low cytotoxicity of the dots. As chemical stability is one of the essential prerequisites for *in vivo* biological applications, the BTF dots were dispersed at different pH and their optical properties were studied as shown in Figure S20 (Supporting Information). No obvious changes in UV and PL are detected in buffer solutions with different pH. The hydrodynamic diameter of the BTF dots in buffer solutions also maintains at the value of 119–134 nm even the pH is varied (Figure S21, Supporting Information). All these results suggest that the BTF dots show high chemical stability, which makes them promising as fluorescent nanoprobe for *in vivo* fluorescence imaging.

To investigate the nonlinear optical property of the BTF dots, a measuring system was built as shown in Figure S22 (Supporting Information). Under NIR-II femtosecond (fs) laser excitation at 1550 nm, three photons of 1550 nm were absorbed simultaneously in the excitation process followed by the same radiative decay pathway as that of one-photon process as suggested by the similarity of the obtained PL spectra (Figure 3B). The bright 3PF of the BTF dots was observed at ≈ 650 nm accompanied with a sharp signal peak from the third-harmonic generation (THG)^[30] at 517 nm (Figure 3B,C). 3PF and THG are both high-order nonlinear optical effects. 3PF is approximate to a fifth-order nonlinear optical effect, while THG is a third-order nonlinear optical effect. Herein, under 1550 nm fs laser excitation, the 3PF signal of the BTF dots is much stronger than their THG signal. Moreover, the 3PF emission maximum locates in FR/NIR region at 650 nm, which is longer than that of THG in green region at 517 nm. Therefore, intense 3PF of the BTF dots is more suitable for *in vivo* bioimaging due to higher penetration depth and lower light absorption in biological tissues. The power dependence of 3PF intensity of the BTF dots on excitation intensity of the 1550 nm fs laser was plotted. The 3PF intensity of the BTF dots is proportional to the cubic power of the excitation intensity at 1550 nm (Figure 3D), which is demonstrative of the main nonlinear optical process of 3PF. The three-photon absorption cross section (σ_3) of the BTF dots was further measured by the three-photon induced fluorescence method. At 1550 nm, the σ_3 of BTF was measured to be $2.56 \times 10^{-79} \text{ cm}^6 \text{ s}^2$, which is much higher than that of commonly used organic dye Rh6G ($6 \times 10^{-81} \text{ cm}^6 \text{ s}^2$)^[31] and some previously reported dyes.^[32] The higher σ_3 value of the BTF dots is advantageous for deep-tissue bioimaging. The photostability

of the BTF dots was investigated by monitoring their PL change upon continuous laser irradiation at 1550 nm (Figure 3E). After 40 min continuous irradiation, the BTF dots maintain more than 90% of their initial 3PF intensity in PBS and aqueous suspension. Such good photostability enables long-term bioimaging applications.

Encouraged by the good 3PF and biocompatibility of the BTF dots, we first investigated the real-time imaging of mouse cerebrovascular through a small cranial window using a 3PF imaging system (Figure S23, Supporting Information). The representative vasculature images of the mouse brain at penetration depths from 0 to 900 μm are shown in Figure S24 (Supporting Information). The intrinsic THG signal generated at various penetration depths was also observed in Figure S25 (Supporting Information), which could provide additional structural information at superficial depths. As shown in Figure 4A–C, the 3PF and THG signals are well-matched and this suggests they origin from the same nanoprobe. The combination of different imaging modes with 3PF and THG enhances the reliability of deep-tissue imaging. Figure 4D–F shows the 3D high resolution reconstruction vasculature images of the mouse brain at various penetration depths from 0 to 900 μm . Careful measurement of the images enables the quantitative analysis of the full width at half maximum (FWHM) of the indicated tiny capillary, which is equal to 1.68 and 1.80 μm at depths of 300 and 600 μm , respectively (Figure 4G,H). The SBRs of the 3PF images at depths of 200, 300, 400, and 500 μm are calculated to be 15.6, 8.9, 5.7, and 5.3, respectively (Figure 4I). The large SBRs are attributed to the high-order nonlinear optical effect^[33] and the strong 3PF signal of the BTF dots as well as good penetration capability of the NIR-II excitation light. The gradual fluorescence loss is attributed to the absorption/scattering of the deep-tissue of mouse brain. Through combination of images at different penetration depths (Figure 4J), high resolution 3D images are reconstructed from different visual angles (Figure 4K,L), which provide a general and clear spatial picture about major blood vasculature networks and details of the tiny capillaries.

Taking the full advantage of 3PF imaging, the fluorescent BTF dots are further utilized for practical applications in visualization of brain blood vessels of mouse with intact skull *in vivo*. The noninvasive operation was shown in Figure S26 (Supporting Information), which could avoid the physiological alternations and the functional interference of the brain. Figure 5A–C, on the other hand, shows the 3D high resolution reconstruction images of the mouse brain vessels, through which an unambiguous spatial picture of the major vascular system and the tiny capillary network is provided. The FWHM of the indicated tiny capillary is calculated to be 0.95 μm at 200 μm depth, 1.59 μm at 300 μm depth, and 2.08 μm at 400 μm depth (Figure 5D–F). The above results demonstrate that the AIE dots are promising nanoprobe for *in vivo* deep-tissue imaging.

The blood flow velocity in brain is one of the important hemodynamic features of brain conditions and can be investigated using the noninvasive approach through-skull 3PF imaging. The BTF dots are dispersed in the blood plasma rather than stained on the red blood cells (RBCs) (Figure S27, Supporting Information) as indicated by the shadows of RBCs

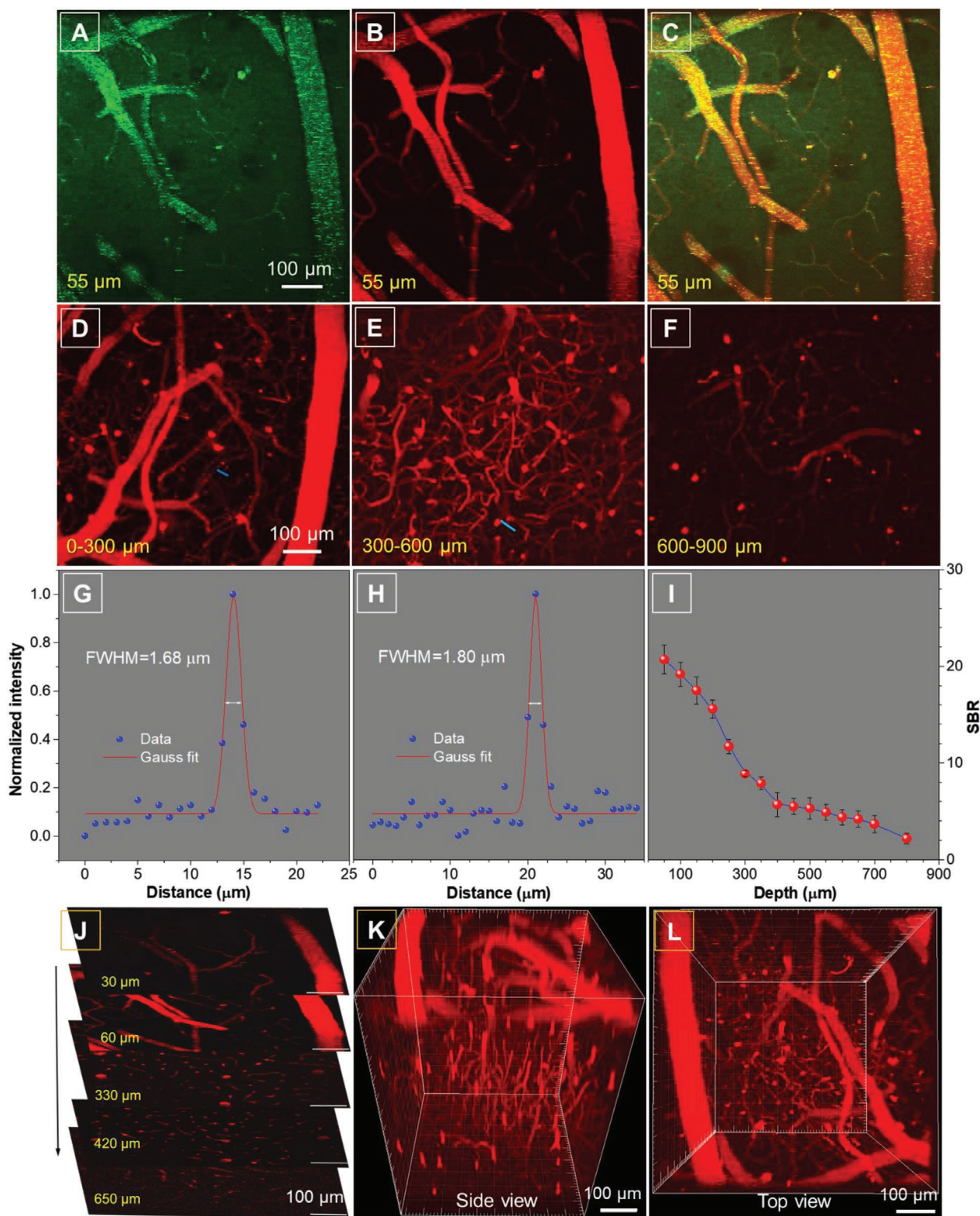


Figure 4. A) THG, B) 3PF, and C) overlay image of the mouse brain vessels at penetration depth of 55 μm. Excitation wavelength: 1550 nm. Scale bar: 100 μm. D–F) In vivo 3D high resolution images of the mouse brain vessels at penetration depth from 0 to 900 μm. G, H) A cross-sectional intensity profile measured along the blue line in (D) and (E). I) Attenuation curve of the fluorescence signal. J) Fluorescence images of the brain vessels at various penetration depths. Scale bar: 100 μm. K) The side and L) top view of the constructed 3D images of the blood vessels of the mouse brain at penetration depth from 0 to 900 μm. Scale bar: 100 μm.

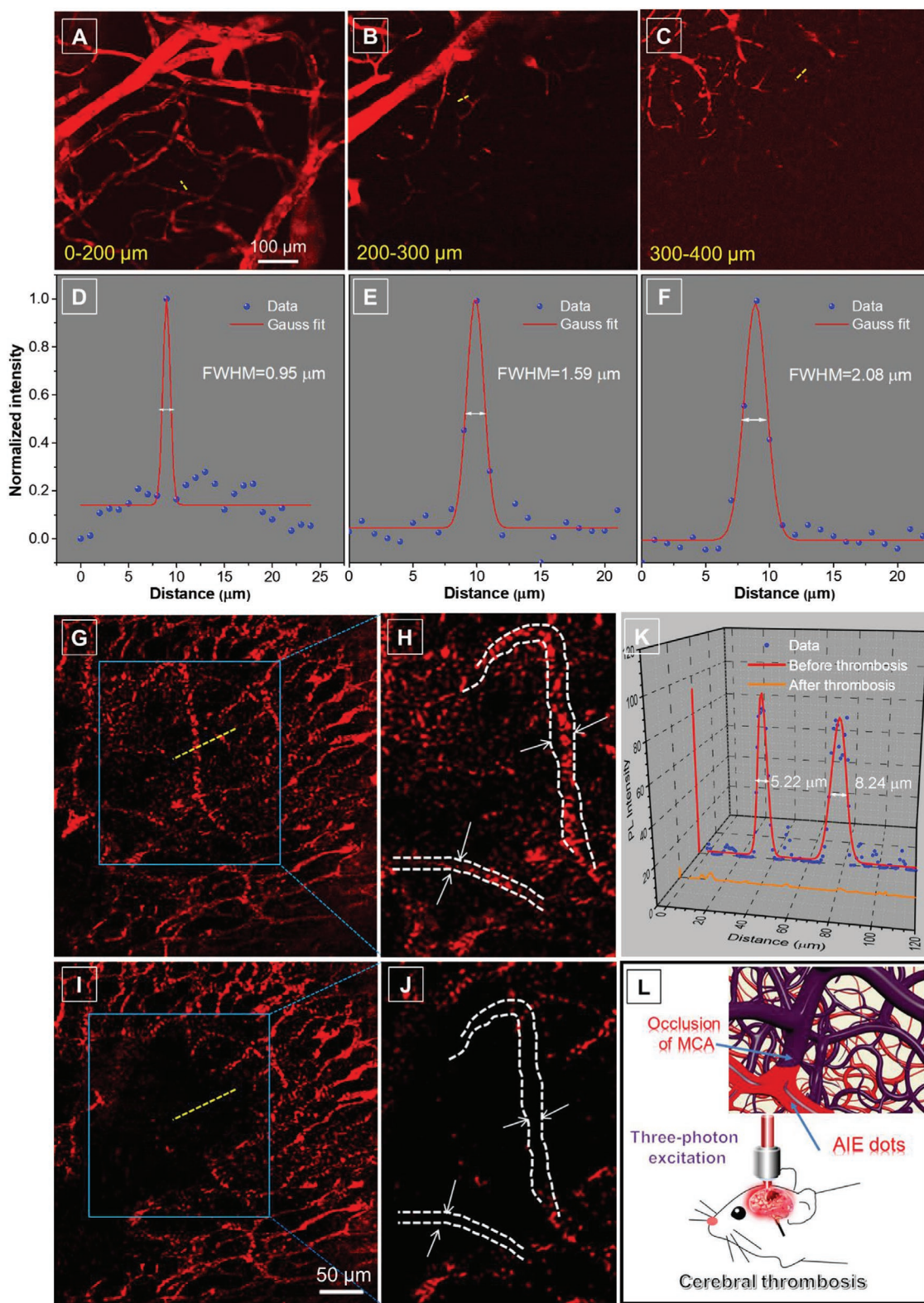


Figure 5. A–C) In vivo 3D high-resolution images of the mouse brain vessels with intact skull at penetration depth from 0 to 400 μm. Excitation wavelength: 1550 nm. Scale bar: 100 μm. D–F) A cross-sectional intensity profile measured along the yellow line in (A)–(C). G–J) 3PF images of brain blood vessels of a mouse with intact skull before (G,H) and after (I,J) brain thrombosis. Scale bar: 50 μm. K) A cross-sectional intensity profile measured along the yellow line in (G) and (I). L) Schematic illustration of the visualization of brain thrombosis process with intact skull based on the AIE dots through the 3PF microscopy imaging technique.

flowing with the fluorescent plasma. Through tracking the distance traveled by the fluorescent spot against time, the average blood flow velocity (dx/dt) of the indicated capillary was calculated to be $\approx 3.8 \text{ mm s}^{-1}$ (Figure S28, Supporting Information), corresponding to a volume blood flow of $1.45 \times 10^{-2} \mu\text{L min}^{-1}$.

Cerebral thrombosis is a prevalent brain disease and can induce acute brain injury and even death. Thus, we further utilized the BTF nanodots to monitor the cerebral stroke process of mouse with intact skull. 3PF imaging of the brain of a mouse with intact skull was first conducted using AIE dots, through which the general information on vasculature structure with a large field of view was obtained (Figure 5G,H) by an infrared antireflection low magnification objective. After metabolism for several hours, no 3PF signal of BTF dots in the brain blood vessels of mouse was observed (Figure S29, Supporting Information). Then a microsurgery was performed on the same mouse to induce occlusion in the origin of the middle cerebral artery (MCA) followed by intravenous injection of the BTF dots. After formation of occlusion of MCA in mouse brain, the indicated brain blood vessels in the right cerebral hemisphere were invisible in the same location (Figure 5I,J) due to the lack of flowing blood. Evidently, the process of cerebral thrombosis was clearly visualized through the intensity change of 3PF signal of the AIE dots. Same conclusion was drawn through quantitative analysis of the highlighted lines in the images (Figure 5K). Strong 3PF signal with a high value of 92.1 from the indicated blood vessels can be effectively monitored in the normal condition of the brain. After formation of cerebral thrombosis, the 3PF intensity is dramatically decreased to a low value of 1.1, which is difficult to distinguish from the background signal. Similar results induced by occlusion of MCA are also observed at the middle of cerebral hemisphere of mouse (Figure S30, Supporting Information). While the mouse without microsurgery was used as control under the same 3PF microscopy imaging condition. No obvious cerebral thrombosis process could be observed (Figure S31, Supporting Information). Therefore, the fluorescence microscopy images reveal the cause of disease through the remarkable difference in 3PF intensity of the cerebral vasculature in complicated central neural system, which significantly benefits for understanding the pathogenesis of brain diseases. In recent years, some luminogens have been synthesized for deep-tissue imaging with good performance by NIR-II laser excitation.^[11b,32,34] Different from these molecules prepared by multistep synthesis (normally 5–7 steps) with complicated chemical structures, the present molecule can be facilely synthesized (2 steps) and possesses a simple chemical structure and a suitable molecular weight. More importantly, the cerebral thrombosis process in a living mouse with intact skull was first visualized noninvasively with high contrast based on ultrabright AIE dots with remarkable nonlinear optical effect (Figure 5L).

In summary, bright AIE luminogens are facilely synthesized. The FR-NIR luminogen namely BTF shows a high quantum efficiency of up to 42.6% in powders. The resulting AIE dots enjoy high brightness, large Stokes shift, good biocompatibility, satisfactory photostability, and large three-photon absorption cross section. They can be utilized as highly efficient fluorescent probes for in vivo brain vascular imaging by NIR-II laser excitation with high penetration depth and image contrast. It is the first report of using AIE dots for the visualization of cerebral

stroke process in mice noninvasively through 3PF microscopy imaging. These good results will shed light on the development of efficient solid-state NIR emitters for noninvasive monitoring disease or dysfunction in brain.

Supporting Information

Supporting Information is available from the Wiley Online Library or from the author.

Acknowledgements

W.Q. and N.A. contributed equally to this work. The financial support was partially received from National Natural Science Foundation of China (21971265, 21374136, 61975172, 61735016, and 21788102), the Fundamental Research Funds for the Central Universities (18lgpy04 and 17lgjc03), the Zhejiang Provincial Natural Science Foundation of China (LR17F050001), the Research Grants Council of Hong Kong (C6009-17G), and the Innovation and Technology Commission (ITC-CNERC14SC01). The authors are grateful to Miss Y. Zhang from Basic Medical Sciences and Mr. L. Zhu from Interdisciplinary Institute of Neuroscience and Technology (ZIINT) in Zhejiang University for their help in animal experiments. The authors are also grateful to Dr. Y. Zhou from School of Chemistry and Chemical Engineering in Guangxi University for Nationalities for analysis of single-crystal structure. The procedures for all the animal experiments were approved by the Institutional Ethical Committee of Animal Experimentation of Zhejiang University in China. They were strictly performed in compliance with the rules of governmental and international guidelines on animal experimentation. According to requirements for Biosafety and Animal Ethics, all efforts were made to minimize the number of animals used and their suffering.

Conflict of Interest

The authors declare no conflict of interest.

Keywords

aggregation-induced emission, cerebral thrombosis, intact skull, NIR-II excitation, three-photon fluorescence imaging

Received: January 16, 2020

Revised: March 30, 2020

Published online:

- [1] Y. Li, Y. Sun, J. Li, Q. Su, W. Yuan, Y. Dai, C. Han, Q. Wang, W. Feng, F. Li, *J. Am. Chem. Soc.* **2015**, *137*, 6407.
- [2] X. Lou, Z. Zhao, B. Z. Tang, *Small* **2016**, *12*, 6430.
- [3] a) S. Wang, F. Hu, Y. Pan, L. G. Ng, B. Liu, *Adv. Funct. Mater.* **2019**, *29*, 1902717; b) D. Ding, C. C. Goh, G. Feng, Z. Zhao, J. Liu, R. Liu, N. Tomczak, J. Geng, B. Z. Tang, L. G. Ng, B. Liu, *Adv. Mater.* **2013**, *25*, 6083.
- [4] F. Helmchen, W. Denk, *Nat. Methods* **2005**, *2*, 932.
- [5] X. Wang, P. Li, Q. Ding, C. Wu, W. Zhang, B. Tang, *J. Am. Chem. Soc.* **2019**, *141*, 2061.
- [6] N. Ji, J. Freeman, S. L. Smith, *Nat. Neurosci.* **2016**, *19*, 1154.
- [7] a) G. Yang, F. Pan, C. N. Parkhurst, J. Grutzendler, W.-B. Gan, *Nat. Protoc.* **2010**, *5*, 201; b) H.-T. Xu, F. Pan, G. Yang, W.-B. Gan, *Nat. Neurosci.* **2007**, *10*, 549; c) Y. Chen, S. Liu, H. Liu, S. Tong, H. Tang,

- C. Zhang, S. Yan, H. Li, G. Yang, D. Zhu, K. Wang, P. Wang, *Anal. Chem.* **2019**, *91*, 9371.
- [8] J.-H. Park, W. Sun, M. Cui, *Proc. Natl. Acad. Sci. USA* **2015**, *112*, 9236.
- [9] D. Wang, J. Qian, in *Principles and Applications of Aggregation-Induced Emission* (Eds: Y. Tang, B. Z. Tang), Springer International Publishing, Cham, Switzerland **2019**, Ch. 18.
- [10] a) T. Wang, D. G. Ouzounov, C. Wu, N. G. Horton, B. Zhang, C.-H. Wu, Y. Zhang, M. J. Schnitzer, C. Xu, *Nat. Methods* **2018**, *15*, 789; b) M. Yildirim, H. Sugihara, P. T. C. So, M. Sur, *Nat. Commun.* **2019**, *10*, 177; c) D. G. Ouzounov, T. Wang, M. Wang, D. D. Feng, N. G. Horton, J. C. Cruz-Hernández, Y.-T. Cheng, J. Reimer, A. S. Tolia, N. Nishimura, C. Xu, *Nat. Methods* **2017**, *14*, 388.
- [11] a) K. Zagorovsky, W. C. W. Chan, *Nat. Mater.* **2013**, *12*, 285; b) S. Wang, J. Liu, G. Feng, L. G. Ng, B. Liu, *Adv. Funct. Mater.* **2019**, *29*, 1808365.
- [12] K. Guesmi, L. Abdeladim, S. Tozer, P. Mahou, T. Kumamoto, K. Jurkus, P. Rigaud, K. Loulier, N. Dray, P. Georges, M. Hanna, J. Livet, W. Supatto, E. Beaufort, F. Druon, *Light: Sci. Appl.* **2018**, *7*, 12.
- [13] a) D. Kim, N. Lee, Y. I. Park, T. Hyeon, *Bioconjugate Chem.* **2017**, *28*, 115; b) J. H. Yu, S.-H. Kwon, Z. Petrášek, O. K. Park, S. W. Jun, K. Shin, M. Choi, Y. I. Park, K. Park, H. B. Na, N. Lee, D. W. Lee, J. H. Kim, P. Schwill, T. Hyeon, *Nat. Mater.* **2013**, *12*, 359.
- [14] G. S. He, L.-S. Tan, Q. Zheng, P. N. Prasad, *Chem. Rev.* **2008**, *108*, 1245.
- [15] A. M. Derfus, W. C. W. Chan, S. N. Bhatia, *Nano Lett.* **2004**, *4*, 11.
- [16] a) A. Aliyan, N. P. Cook, A. A. Martí, *Chem. Rev.* **2019**, *119*, 11819; b) J. Zhang, X. Chai, X.-P. He, H.-J. Kim, J. Yoon, H. Tian, *Chem. Soc. Rev.* **2019**, *48*, 683.
- [17] T. L. Mako, J. M. Racicot, M. Levine, *Chem. Rev.* **2019**, *119*, 322.
- [18] a) S. Xu, Y. Duan, B. Liu, *Adv. Mater.* **2020**, *32*, 1903530; b) C. Wang, Z. Li, *Mater. Chem. Front.* **2017**, *1*, 2174; c) H. Gao, X. Zhang, C. Chen, K. Li, D. Ding, *Adv. Biosyst.* **2018**, *2*, 1800074; d) D. Wang, M. M. S. Lee, G. Shan, R. T. K. Kwok, J. W. Y. Lam, H. Su, Y. Cai, B. Z. Tang, *Adv. Mater.* **2018**, *30*, 1802105; e) M. Chen, R. Chen, Y. Shi, J. Wang, Y. Cheng, Y. Li, X. Gao, Y. Yan, J. Z. Sun, A. Qin, R. T. K. Kwok, J. W. Y. Lam, B. Z. Tang, *Adv. Funct. Mater.* **2018**, *28*, 1704689; f) C. Chen, X. Ni, S. Jia, Y. Liang, X. Wu, D. Kong, D. Ding, *Adv. Mater.* **2019**, *31*, 1904914; g) C. Chen, H. Ou, R. Liu, D. Ding, *Adv. Mater.* **2020**, *32*, 1806331.
- [19] a) J. Mei, Y. Huang, H. Tian, *ACS Appl. Mater. Interfaces* **2018**, *10*, 12217; b) W. Qin, P. Zhang, H. Li, J. W. Y. Lam, Y. Cai, R. T. K. Kwok, J. Qian, W. Zheng, B. Z. Tang, *Chem. Sci.* **2018**, *9*, 2705; c) X. Ni, X. Zhang, X. Duan, H.-L. Zheng, X.-S. Xue, D. Ding, *Nano Lett.* **2019**, *19*, 318.
- [20] Y. Wang, M. Chen, N. Alifu, S. Li, W. Qin, A. Qin, B. Z. Tang, J. Qian, *ACS Nano* **2017**, *11*, 10452.
- [21] T. Savić, G. Gambino, V. S. Bokharraie, H. R. Noori, N. K. Logothetis, G. Angelovski, *Proc. Natl. Acad. Sci. USA* **2019**, *116*, 20666.
- [22] H. Monai, X. Wang, K. Yahagi, N. Lou, H. Mestre, Q. Xu, Y. Abe, M. Yasui, Y. Iwai, M. Nedergaard, H. Hirase, *Proc. Natl. Acad. Sci. U. S. A.* **2019**, *116*, 11010.
- [23] a) M. F. Kircher, A. de la Zerda, J. V. Jokerst, C. L. Zavaleta, P. J. Kempen, E. Mittra, K. Pitter, R. Huang, C. Campos, F. Habte, R. Sinclair, C. W. Brennan, I. K. Mellinghoff, E. C. Holland, S. S. Gambhir, *Nat. Med.* **2012**, *18*, 829; b) C. Zhao, L. Lai, F. U. Rehman, C. Qian, G. Teng, H. Jiang, X. Wang, *RSC Adv.* **2016**, *6*, 110525.
- [24] Z. Sheng, B. Guo, D. Hu, S. Xu, W. Wu, W. H. Liew, K. Yao, J. Jiang, C. Liu, H. Zheng, B. Liu, *Adv. Mater.* **2018**, *30*, 1800766.
- [25] a) J. Mei, Y. Hong, J. W. Y. Lam, A. Qin, Y. Tang, B. Z. Tang, *Adv. Mater.* **2014**, *26*, 5429; b) W. Qin, Z. Yang, Y. Jiang, J. W. Y. Lam, G. Liang, H. S. Kwok, B. Z. Tang, *Chem. Mater.* **2015**, *27*, 3892.
- [26] Z. R. Grabowski, K. Rotkiewicz, W. Rettig, *Chem. Rev.* **2003**, *103*, 3899.
- [27] S. Sasaki, G. P. C. Drummen, G.-I. Konishi, *J. Mater. Chem. C* **2016**, *4*, 2731.
- [28] R. Hu, E. Lager, A. Aguilar-Aguilar, J. Liu, J. W. Y. Lam, H. H. Y. Sung, I. D. Williams, Y. Zhong, K. S. Wong, E. Peña-Cabrera, B. Z. Tang, *J. Phys. Chem. C* **2009**, *113*, 15845.
- [29] W. Lin, L. Yuan, Z. Cao, Y. Feng, J. Song, *Angew. Chem., Int. Ed.* **2010**, *49*, 375.
- [30] a) J. A. Squier, M. Müller, G. J. Brakenhoff, K. R. Wilson, *Opt. Express* **1998**, *3*, 315; b) Y. Barad, H. Eisenberg, M. Horowitz, Y. Silberberg, *Appl. Phys. Lett.* **1997**, *70*, 922.
- [31] G. Xing, S. Chakraborty, S. W. Ngiam, Y. Chan, T. C. Sum, *J. Phys. Chem. C* **2011**, *115*, 17711.
- [32] A. K. Mandal, S. Sreejith, T. He, S. K. Maji, X.-J. Wang, S. L. Ong, J. Joseph, H. Sun, Y. Zhao, *ACS Nano* **2015**, *9*, 4796.
- [33] N. G. Horton, K. Wang, D. Kobat, C. G. Clark, F. W. Wise, C. B. Schaffer, C. Xu, *Nat. Photonics* **2013**, *7*, 205.
- [34] a) S. Wang, J. Liu, C. C. Goh, L. G. Ng, B. Liu, *Adv. Mater.* **2019**, *31*, 1904447; b) H. Zhang, N. Alifu, T. Jiang, Z. Zhu, Y. Wang, J. Hua, J. Qian, *J. Mater. Chem. B* **2017**, *5*, 2757; c) J. Qian, Z. Zhu, A. Qin, W. Qin, L. Chu, F. Cai, H. Zhang, Q. Wu, R. Hu, B. Z. Tang, S. He, *Adv. Mater.* **2015**, *27*, 2332.